Electrochimica Acta 318 (2019) 937–948

Contents lists available at ScienceDirect

Electrochimica Acta

journal homepage: www.elsevier.com/locate/electacta

Highly faceted layered orientation in SnSSe nanosheets enables facile Li^+-Diffusion channels

Xusheng Wang [a, b, *, 1], Chang Li [c, *, 1], Chunyi Liu [c], Luxiang Ma [b], Rui Li [c], Jitao Chen [b, *], Mianqi Xue [a]

[a] Technical Institute of Physics and Chemistry, Chinese Academy of Sciences, Beijing, 100190, China
[b] Beijing National Laboratory for Molecular Sciences College of Chemistry and Molecular Engineering, Peking University, Beijing, 100871, China
[c] School of Advanced Materials, Peking University Shenzhen Graduate School, Shenzhen, 518055, China

ARTICLE INFO

Article history:
Received 30 April 2019
Received in revised form
31 May 2019
Accepted 8 June 2019
Available online 15 June 2019

Keywords:
Faceted growth
Layered orientation
SnSSe
Graphene
Lithium-ion storage

ABSTRACT

Main attention to the interlayer regulation of layered metal chalcogenides (LMCs) is focused on the expansion of interlayer spacing to improve the Li^+-storage performance. However, the issues of poor material homogeneity and complicated preparation make this strategy incapable to realize a wider application. In this work, a new interlayer design of the oriented growth of layered (00*l*) facets enables facile Li^+-diffusion channels in SnSSe nanosheets. The further assembly between SnSSe nanosheets and reduced graphene oxide (SnSSe/rGO) generates flexible freestanding electrodes, in which the SnSSe nanosheets are tiled onto the rGO nanolayers with a planar configuration. The SnSSe/rGO electrodes demonstrate an ultrahigh discharge capacity of 2049 mAh g^{-1} at 0.1 A g^{-1} (based on the active mass of SnSSe) and a considerable capacity retention of 82% after 2000 cycles at 1 A g^{-1}. The morphological characterization of long-life cycled SnSSe/rGO electrode confirms an open structure built with vertical lamellas, which can provide more active sites and accommodate the volume expansion–contraction of SnSSe nanosheets.

1. Introduction

The combination of new clean energy and lithium-ion battery (LIB) has become a trend for energy storage and application [1]. And further advancement of LIB needs the exploitation of high-performance anode materials [2–5]. Layered metal chalcogenides (LMCs) with MoS_2, WS_2, and SnS_2 as the representatives have been of significant interest as the anodes of LIB, due to their advantages of high theoretical capacity, low cost, and facile design of size and morphology [6–12]. The Li^+ insertion into interlayer and the following conversion reaction along the interlayer (additional alloying reaction for the SnS_2) provide main contribution to the whole capacity delivery [13–16]. Therefore, the interlayer regulation is a key consideration for optimizing the capacity delivery and cycling stability of these LMCs [17,18].

The widely used method to realizing a stable Li^+-insertion process is the expansion of interlayer spacing, which plays a positive role in volume accommodation and transportation kinetics of LMCs [19,20]. This design to reduce the Li^+-insertion barrier mainly depends on the weakening of van der Waals interaction. In this case, it is feasible to realize monolayer (or multilayer) electrochemical behavior, which allows more accessible active Li^+-storage sites and more resistance to the structural pulverization compared to that of the bulk LMCs with a narrower interlayer spacing [21]. Efforts to achieve the expanded interlayer spacing are mainly focused on the MoS_2 nanosheets [9,22–25]. Which always demonstrate considerable Li^+-storage capacity delivery and cycling stability. However, most approaches to expanding the interlayer spacing of LMCs need heterogeneous doping or intercalation (metal atoms, metal ions, small molecules/polymers, etc.), of which the physical and chemical homogeneity, facile tunability of particle size, easy synthesis, and large-scale production still remain to be improved [26]. Therefore, the challenge is to combine the strategy of interlayer-spacing expansion with novel designs that can further improve the Li^+-storage performance of LMCs [27].

* Corresponding authors. Technical Institute of Physics and Chemistry, Chinese Academy of Sciences, Beijing, 100190, China.
E-mail addresses: wangxs@mail.ipc.ac.cn (X. Wang), lirui@pkusz.edu.cn (R. Li), chenjitao@pku.edu.cn (J. Chen).
[1] X.S.W. and C.L. contributed equally to this work. All authors have given approval to the final version of the manuscript.

https://doi.org/10.1016/j.electacta.2019.06.041
0013-4686/

The tailored crystal growth with desirable facets has triggered a high level of interest in synthesizing functional materials in many fields (sensor, catalysis, etc.) [28–31]. Therefore, the oriented growth of (00*l*) facets in LMCs can be used to fabricate better electrode materials, by creating a favorable Li^+-insertion environment with the direct exposure to electrolyte [23]. Generally, layered hexagonal SnS_2 and $SnSe_2$ have high theoretical capacities through the combination of Li^+ insertion, conversion reaction, and alloying reaction, all of which rely on the interlayer regulation regarding the interlayer spacing and the layered orientation of (001) facet [32]. However, the growth of (001) facet is strongly competed by the (101) facet in SnS_2 and the (011) facet in $SnSe_2$ during the synthetic processes especially using solid-state reaction, which allows high crystal homogeneity and large-scale production [33,34]. Herein, we realize the tailored growth of (001) facet in the layer-oriented SnSSe nanosheets with a large interlayer spacing of 0.61 nm and the highly suppressed (101) and (011) facets, thus enabling facile Li^+-diffusion channels. Further assembly with reduced graphene oxide (rGO) produces flexible freestanding SnSSe/rGO nanocomposite electrodes with an order-stacked structure, wherein the SnSSe nanosheets show a tiled configuration onto the planar extended rGO nanolayers. The SnSSe/rGO electrodes deliver an ultrahigh specific capacity of 2049 mAh g^{-1} at 0.1 A g^{-1} for the active mass of SnSSe and a remarkable capacity retention of 82% after 2000 cycles at 1 A g^{-1}. The long-life cycled SnSSe/rGO electrode reveals a unique open structure built with vertical lamellas, which is favorable to the full use of active sites and the accommodation of volume expansion–contraction of the SnSSe nanosheets.

2. Experimental section

2.1. Synthesis of the SnSSe materials

The single-crystal SnSSe was synthesized by mixing Sn powders (Alfa Aesar, 99.8%), S powders (Alfa Aesar, 99.5%), and Se powders (Alfa Aesar, 99+%) with a molar ratio of 1 : 1: 1 and then reacting at 900 °C for 20 h with slow heating and cooling procedures under a vacuum environment in a sealed silica tube. The polycrystal SnSSe was synthesized at 400 °C for 50 h with relatively rapid heating and cooling procedures.

2.2. Synthesis of the GO material

2 g expanded graphite was added to a clean beaker (1000 mL), and then 92 g concentrated sulfuric acid was slowly dumped into the above beaker, which was then covered closely by using a sealing film. After being stirred for 24 h (200 rpm), 1 g $NaNO_3$ was added to the concentrated sulfuric acid dispersion with 5 min stirring process. Then 6 g $KMnO_4$ was very slowly added to the above dispersion under an ice bath with a stirring process (5 min). Then the beaker kept stirring for 30 min in a water bath (35 °C). After that, 5 mL water was added to the beaker along the wall with a stirring process (5 min). Then another 5 mL water was added again with a stirring process (5 min). After that, 40 mL water was added to the dispersion at 350 rpm with a stirring process (5 min). Then 400 mL water was added to the dispersion and kept stirring at 750 rpm with a stirring process (5 min). After that, 20 mL fresh H_2O_2 (35%) was poured into the beaker and kept stirring with a stirring process (5 min). After that, natural settlement of the dispersion was performed for 2 h. Then the supernatant was sucked out and the concentrated dispersion was washed by hydrochloric acid solution twice. Then the GO dispersion in water was collected by centrifugation.

2.3. Preparation of the single-crystal SnSSe, polycrystal SnSSe, rGO, and SnSSe/rGO electrodes

The bulk single-crystal and polycrystal SnSSe samples were firstly grinded. Then the two kinds of powders were separately mixed with carbon black and sodium carboxymethylcellulose (CMC) at a weight ratio of 75 : 15: 10. The two kinds of slurries were spread on the Cu foils and dried at 75 °C, then the two foils were cut into electrode disks with a diameter of 11 mm and dried at 75 °C over 12 h under vacuum. The single-crystal SnSSe powders were further ball milled by adding distilled water. After ball-milling treatment, the slurry was centrifuged (TG16-WS, 5000 r/min) and supernatant was collected and treated with ultrasound (SB-5200DTDN, 100 W, 40 KHz) for 1 h to obtain the SnSSe aqueous dispersion. The SnSSe aqueous dispersion (2.5 mg mL^{-1}) was mixed with the GO aqueous dispersion (2.0 mg mL^{-1}) at a mass ratio of 1 : 1 (SnSSe: GO) and the mixed dispersion diluted with water to 15 mL. And then the mixed dispersion was treated with ultrasound in cold water (below 10 °C) for 1 h. After that, it was frozen at −80 °C for 2 h. The sample was then freeze-dried for 40 h to obtain the SnSSe/GO foams. The prepared SnSSe/GO foams were pressed into the flexible films and then tailored into disks to obtain the SnSSe/GO electrodes, which were further reduced at 300 °C for 6 h under Ar/H_2 atmosphere (H_2 is 5 vol%) to obtain the SnSSe/rGO electrodes. The rGO electrodes were prepared by using the same procedures of SnSSe/rGO electrodes without the introduction of SnSSe [35]. The contents of SnSSe and rGO were separately fitted to be 67 wt% and 33 wt% by using an Elemental Analyzer.

2.4. Material characterizations

The crystal structures of SnSSe and SnSSe/rGO were characterized by X-ray diffraction (XRD, Bruker D8 Advance diffractometer) with Cu K_α radiation ($\lambda = 1.5405$ Å). The thickness of SnSSe nanosheets was characterized by atomic force microscope (AFM, Veeco Multimode III). The morphology and size of obtained samples and cycled electrodes were examined by scanning electronic microscopy (SEM, ZEISS Supra 55, with the energy-dispersive X-ray spectroscopy (EDX) test) and transmission electron microscopy (TEM, FEI Tecnai G2 F20 s-Twin). The surface chemical states were assessed by X-ray photoelectron spectroscopy (XPS, ESCALAB 250Xi, Thermo Fisher Ltd.). The Raman spectra of obtained samples were recorded using a Raman spectrometer (iHR320, HORIBA Jobin Yvon). The contents of SnSSe and rGO were determined by using an Elemental Analyzer (vario EL, Elementar Analysensysteme GmbH).

2.5. Electrochemical test

The half-cell performance were characterized with lithium metal foils as the counter electrodes, glass fibers as the separators, and 1 mol L^{-1} $LiPF_6$ in EC/DMC/EMC (v: v: v = 1 : 1: 1) as the electrolyte, and then assembled into LIR2032-type coin cells in an argon-filled glove box. All the SnSSe/rGO and rGO electrodes were cycled at a small current density until the stable state was achieved (activation process). And the statistics of cycle number start after the activation process. The average mass loading of SnSSe/rGO is 1.5 mg cm^{-2}. Cyclic voltammetry (CV) and electrochemical impedance spectroscopy (EIS, from 100 kHz to 10 mHz) tests were performed on an Autolab electrochemical system. The battery tests were carried out by using a battery test system (LANDdt) within a voltage range of 0.01–3.0 V versus Li^+/Li.

3. Results and discussion

Bulk single-crystal SnSSe was synthesized via a solid-state

reaction using stoichiometric tin, sulfur, and selenium powders [36,37]. Its XRD pattern (Fig. S1, Supporting Information) only shows the layered-structure-related (00*l*) peaks, suggesting its single-crystal feature. Its morphology was evaluated by SEM and then demonstrated in Fig. S2a (Supporting Information). A typical layered configuration built by tightly accumulated lamellas is displayed. The inset exhibits the front SEM image of bulk single-crystal SnSSe. The micron-scale lamellas reveal the smooth surface and interlaced edge, and their stacked module is highly ordered along the direction of layered orientation, indicating the tailored growth of (001) facet. In contrast, the SEM image of polycrystal SnSSe (Fig. S2b, Supporting Information) illustrates the irregular particle size and morphology. The distinct comparison of diffraction spots between the selected area electron diffraction (SAED) patterns of single-crystal SnSSe and polycrystal SnSSe (Fig. S3, Supporting Information) also confirms the conclusion of single crystal. The SnSSe nanosheets were prepared by the wet ball-milling of bulk single-crystal SnSSe. As shown in Fig. 1a, the TEM image was collected to characterize their microstructure. The nanosheets distribute in a planar way, and their thickness is determined to be below 2 nm by AFM topography image (Fig. S4, Supporting Information). The XRD pattern of SnSSe nanosheets is shown in Fig. 1b. Several main diffraction peaks are located at 14.6°, 31.2°, 40.6°, 44.7°, and 60.9°, which can be assigned to the (001), (011), (012), (003), and (004) crystal facets, respectively. Layered-structure-related (001), (003), and (004) peaks are clearly visible in the pattern with a fitted large interlayer spacing of 0.61 nm. And the (001) peak replaces the (101) and (011) peaks as the strongest peak compared to the standard pattern (ICSD no. 98-060-1191). The contrasting difference in peak intensity between the (001) and (101)/(011) facets affirms the preferential growth of (001) facet. The structural schematic of SnSSe nanosheet is exhibited in Fig. 1c. The open side channels perpendicular to the *c*-axis (the orientation of (00*l*) facet) can enable facile Li^+ insertion.

The intrinsic characteristic of poor electronic conductivity in tin chalcogenides restricts the capacity delivery and rate capability

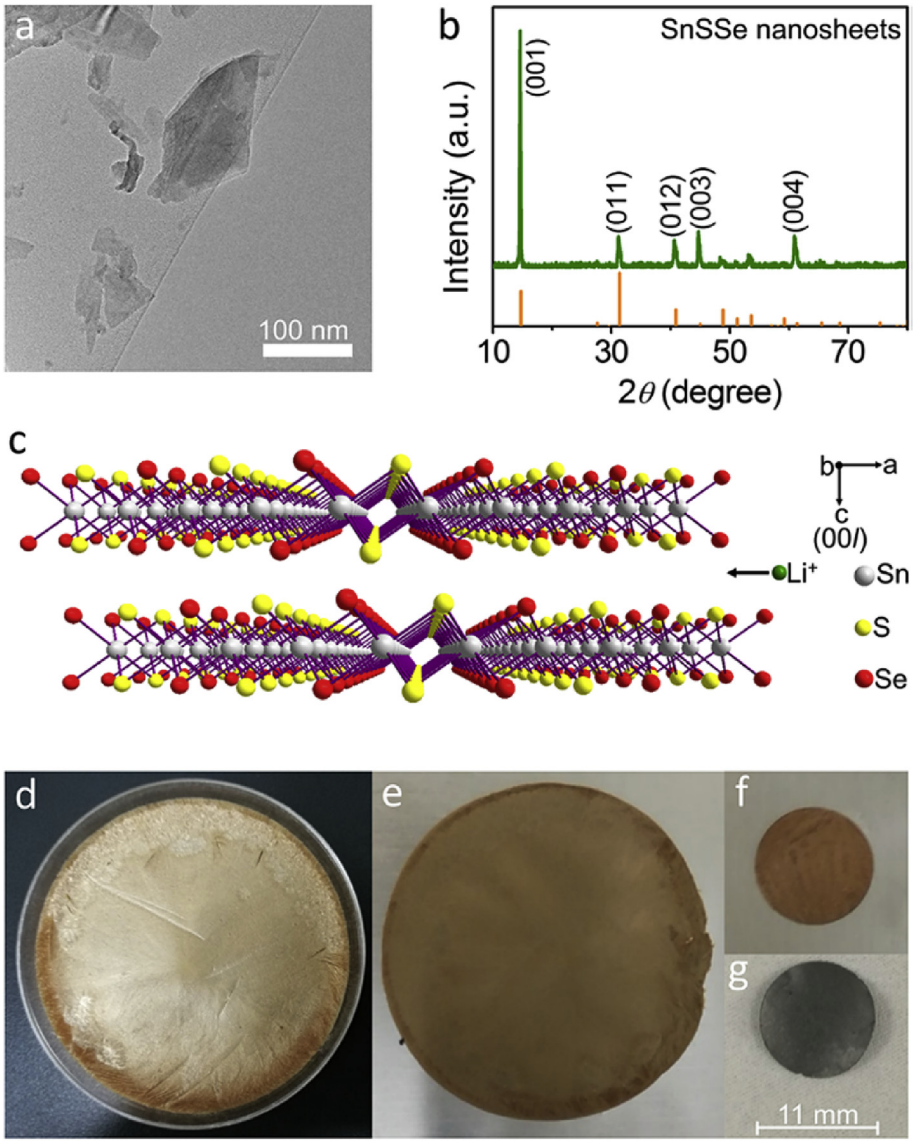

Fig. 1. Oriented growth of the (001) facet in the SnSSe nanosheets and preparation of the SnSSe/rGO electrode. (a) TEM image of the SnSSe nanosheets. A typical laminar configuration is displayed. (b) XRD pattern of the SnSSe nanosheets. Highly oriented growth of the (001) facet is realized. (c) Structural schematic of the SnSSe nanosheets with a Li^+-insertion direction. Images of the SnSSe/GO foam before (d) and after (e) a press treatment. Images of the SnSSe/GO (f) and SnSSe/rGO (g) electrodes. The reduction of GO into rGO does not change the morphology and size.

[38]. The assembly with rGO conductive network into flexible freestanding electrode (SnSSe/rGO) can enhance the electronic transportation kinetics and buffer the volume expansion. Uniform SnSSe/GO composite was prepared by ultrasonic and then freeze-drying methods, and its appearance image is displayed in Fig. 1d, in which GO nanolayers hybridize with SnSSe nanosheets into a brown sponge-like framework. Then it was pressed into a flexible thin film to improve the electronic contact by generating an open compact structure of GO nanolayers (Fig. 1e). Flexible freestanding SnSSe/GO electrode disks (Fig. 1f) were tailored without structural fragmentation. After the reduction of GO, the SnSSe/rGO electrodes were prepared with the maintenance of high flexibility (Fig. 1g).

Under the condition of rGO assembly, the SnSSe nanosheets also depict the oriented domination of (001) facet, which is confirmed by the XRD pattern of SnSSe/rGO electrode (Fig. 2a). The side morphology of SnSSe/rGO electrode was characterized by SEM. As displayed in Fig. 2b, an order-stacked structure assembled by the layer-by-layer rGO-SnSSe sheets is demonstrated with the concomitant interlayer gaps, which can enable facile Li^+-diffusion channels along with the extended rGO nanolayers. The front SEM image of SnSSe/rGO electrode is displayed in Fig. S5 (Supporting Information), in which the SnSSe nanosheets cling closely to the surface of rGO. The micro-structure and -topography of SnSSe/rGO electrode were evaluated by TEM, and the image is displayed in Fig. 2c. Both the size and shape distributions of SnSSe nanosheets are nonuniform with an average diameter of below 500 nm. The ultrathin SnSSe nanosheets are assembled in a tiled way and form a planar morphology onto the rGO nanolayer. The SnSSe nanosheets are encapsulated inside each rGO nanolayer, the high elasticity and electrical conductivity of which can accommodate the volume expansion–contraction [39]. The HRTEM image of SnSSe/rGO electrode is displayed in Fig. 2d. Clear lattice fringes confirm the high crystallinity of SnSSe nanosheets and fine lattice spacing of 0.304 nm is labeled, which can be indexed to the (002) crystal facet. Therefore, layer-related faceted growth along the *c*-axis orientation in the SnSSe nanosheets is further proved. Structural design of the direct exposure of (00*l*) facets and the ordered flexible framework can enable facile Li^+-diffusion channels.

Surface chemical states of the SnSSe/rGO electrode was assessed by using XPS technology. As shown in Fig. 3a, the strong C signal derived from the rGO matrix and the Sn, S, and Se signals derived from SnSSe nanosheets are recognized and marked. The peak-fitting deconvolution curves of C 1s region (Fig. 3b) illustrate three peaks, one should be assigned to the carbon-related C–C bond (284.5 eV) and another two should be assigned to the oxygen-related C–O (285.6 eV) and C=O (288.6 eV) bonds. As displayed in Fig. 3c, the Sn 3d region demonstrates a valence state of Sn^{4+} in the SnSSe nanosheets by the deconvolution of Sn $3d_{3/2}$ and Sn $3d_{5/2}$ peaks. The S 2p and Se 3d XPS regions are demonstrated in Fig. S6 (Supporting Information). The valence states of S^{2-} and Se^{2-} are verified. Raman spectroscopic analyses were also carried out to study the chemical state of SnSSe/rGO electrode. As displayed in Fig. 3d, the intensity ratio of D (1350 cm^{-1}) and G (1586 cm^{-1}) peaks (I_D/I_G) in the SnSSe/rGO electrode is simulated to be 1.01. And in the Raman spectroscopy pattern of SnSSe/GO (Fig. S7, Supporting Information), its I_D/I_G value is fitted to be 0.90,

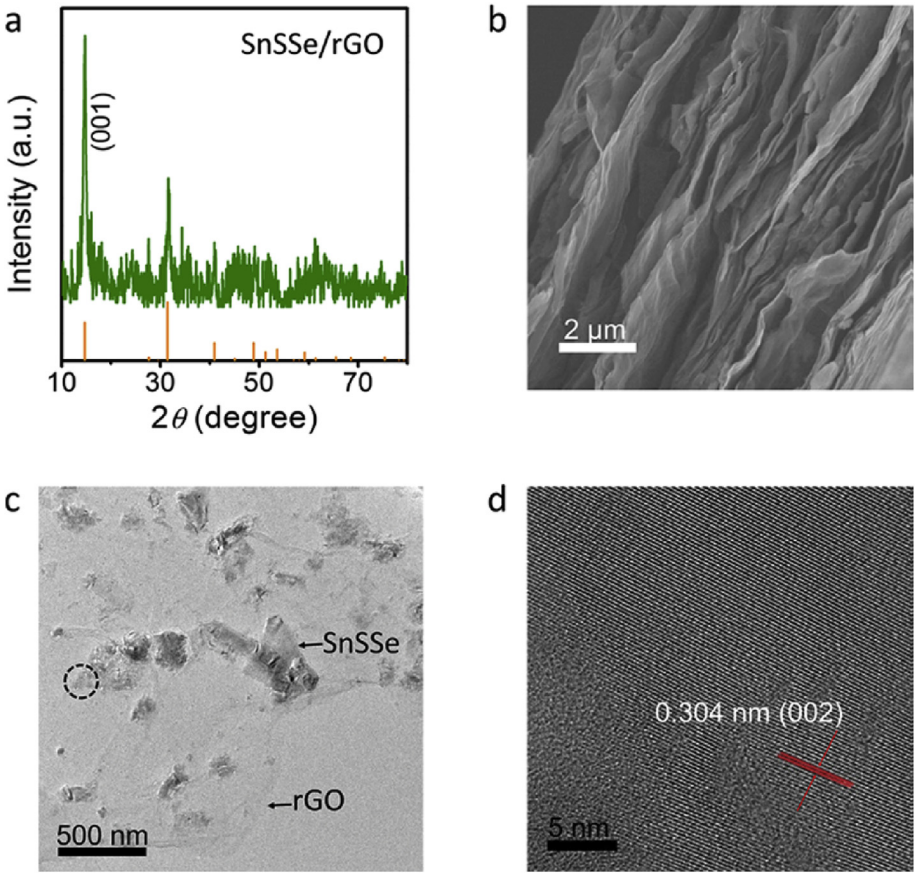

Fig. 2. Faceted layered (001) orientation in the SnSSe/rGO electrode. (a) XRD pattern of the SnSSe/rGO electrode. (b) Side SEM image of the SnSSe/rGO electrode. It reveals an order-stacked structure. (c) TEM image of the SnSSe/rGO electrode. The average diameter of SnSSe nanosheets is below 500 nm. (d) HRTEM image of the SnSSe/rGO electrode taken from the region of dotted circle in panel (c). The labeled lattice spacing of 0.304 nm can be assigned to the (002) facet.

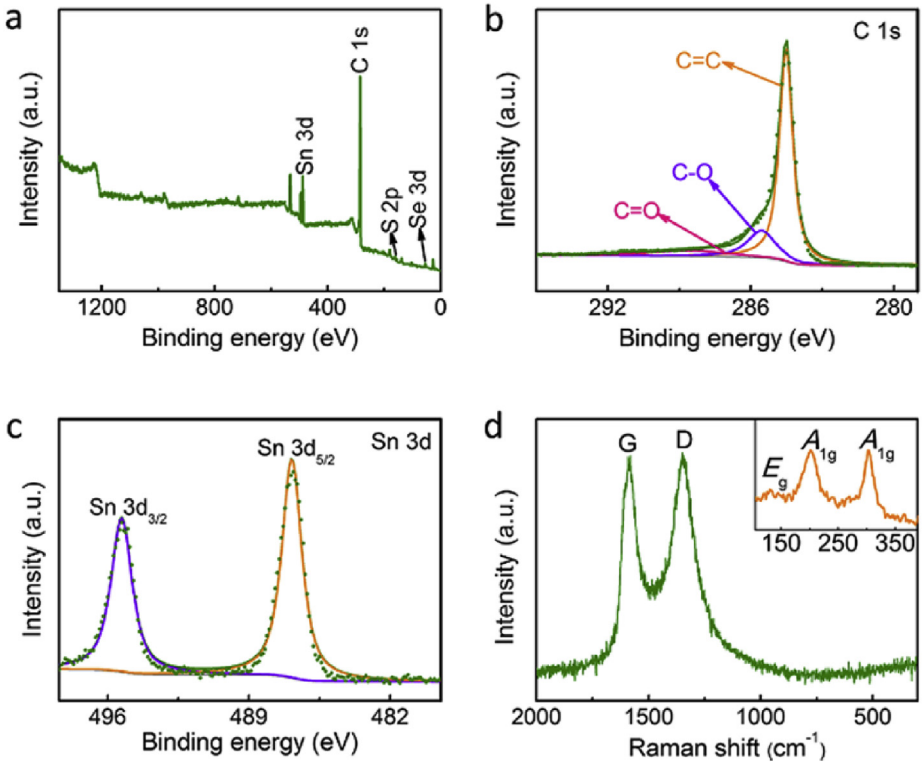

Fig. 3. Spectroscopic characterizations of the SnSSe/rGO electrode. (a) Survey XPS spectrum of the SnSSe/rGO electrode. C 1s (b) and Sn 3d (c) XPS regions of the SnSSe/rGO electrode. (d) Raman spectrum of the SnSSe/rGO electrode. The inset shows the characteristic Raman peaks of SnSSe.

which manifests the successful reduction of GO. The inset of Fig. 3d shows the Raman shift region of SnSSe, in which its characteristic E_g and A_{1g} peaks are confirmed [40].

Electrochemical performance was characterized by using coin-cell tests. The oriented growth of layered (001) facet is more preponderant in the single-crystal SnSSe compared to that of the polycrystal SnSSe, which can be concluded from the two contrastive XRD patterns [36]. And the further comparison of cycling performance (Fig. S8, Supporting Information) demonstrates that the more exposed (001) facet in the single-crystal SnSSe leads to higher capacity delivery and cycling stability. The multi-oriented crystalline grains of polycrystal SnSSe can hinder the electron transfer, which is induced by the electron scattering within the defects and boundaries of SnSSe particles, thus leading to the poorer cycling stability compared to the single-crystal SnSSe with well-oriented crystalline facets. This phenomenon has been demonstrated by the previous work of layered SnS_2 [41]. By subtracting the capacity contribution of rGO species (Fig. S9, Supporting Information), the long-term cycling stability of SnSSe/rGO electrode was assessed at a current density of 1 A g^{-1}. As exhibited in Fig. 4a, a high 1st-cycle discharge capacity of 1408 mAh g^{-1} is achieved for the active mass of SnSSe, which corresponds to 1013 mAhg^{-1} for the SnSSe/rGO composite (the specific formulas are shown in Fig. S10, Supporting Information). Furthermore, a considerable discharge capacity of 1133 mAh g^{-1} is realized for the active mass of SnSSe after 2000 cycles with a high capacity retention of 82%. In Fig. 4b, the current density was then adjusted to 0.1 A g^{-1} to evaluate the capacity delivery of SnSSe/rGO electrode (this statistics of cycle number begins after the long-term cycling test at 1 A g^{-1}). The active mass of SnSSe presents an ultrahigh 1st-cycle discharge capacity of 2049 mAh g^{-1} (1474 mAh g^{-1} for the SnSSe/rGO composite) and a considerable capacity retention of 92% after 200 cycles. The cell performance of SnSSe/rGO electrodes is compared with that of some tin chalcogenides as the LIB anodes [34,38,42–49], which are summarized in Table 1.

The EIS test was implemented to study the kinetics of SnSSe/rGO electrode before and after cycling. As displayed in Fig. 4c, the top inset demonstrates the equivalent circuit, in which the R_b, R_{ct}, Z_w, and C_{dl} separately represent the bulk resistance, charge-transfer resistance, Warburg impedance, and constant phase element [50]. Therefore, the R_{ct} value of the SnSSe/rGO electrode before cycling is smaller than that of the SnSSe/rGO electrode after cycling, indicating an improved kinetics after the cycling test. The stabilization of the electrode/electrolyte interface can decrease the value of R_{ct} [51]. Compared with the EIS patterns of SnSSe electrode (Fig. S11, Supporting Information), its R_{ct} values before and after cycling are both larger than that of the SnSSe/rGO electrode, implying the positive effect of rGO in electronic conductivity. The specific fitted R_{ct} values of SnSSe/rGO and SnSSe electrodes are displayed in Table S1 (Supporting Information). CV curves of the SnSSe and SnSSe/rGO electrodes executed at 0.2 mV s^{-1} are demonstrated in Fig. S12 (Supporting Information). It can be seen that the Li^+-insertion peak in the SnSSe electrode does not appear in the SnSSe/rGO electrode, and this phenomenon should be attributed to the masking effect of rGO, which has been demonstrated in some previously reported rGO-based SnS_2 materials [32,52]. The cathodic peak of SnSSe/rGO electrode located at 1.23 V can be assigned to the conversion reaction with the intermediate products of metallic Sn and Li_2S/Li_2Se, and the following peak located below 0.7 V corresponds to the alloying reaction with the final products of Li_xSn alloys. During the following charge process of SnSSe/rGO electrode, the anodic peak located at 0.63 V can be assigned to the reversible dealloying reaction, and the following peak located at 1.92 V corresponds to the reappearance of tin chalcogenide. The voltage hysteresis of alloying/dealloying reaction in the SnSSe/rGO electrode is 0.41 V, which is smaller than the value of 0.51 V in the

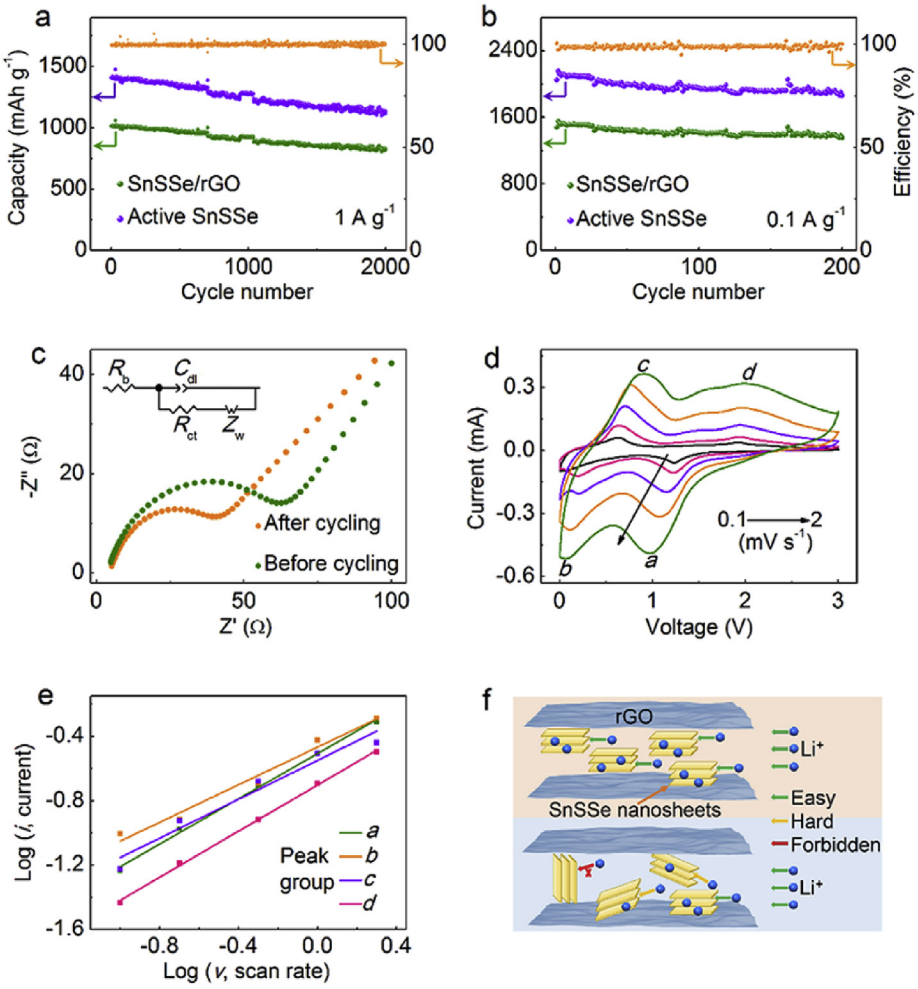

Fig. 4. Electrochemical performance of the SnSSe/rGO electrode. (a,b) Cycling performance of the SnSSe/rGO electrode performed at 1 and 0.1 A g^{-1}, respectively. (c) EIS patterns of the SnSSe/rGO electrode before and after cycling. The inset is the corresponding equivalent circuit. (d) CV curves of the SnSSe/rGO electrode performed at different scan rates within a voltage range of 0.01–3 V. (e) Linear relation of log(v) and log(i) based on the CV tests of SnSSe/rGO electrode. (f) Schematic processes of the Li^+ diffusion within the rGO interlayers and the Li^+ insertion into the SnSSe interlayers with a comparison between the oriented-growth SnSSe nanosheets and disordered-growth SnSSe nanosheets.

Table 1
Comparison of the SnSSe/rGO electrode versus some reported tin chalcogenides as LIB anodes.

Sample	Capacity	Capacity retention	Ref.
SnSSe/rGO	1474 mAh g^{-1} at 0.1 A g^{-1}	82.0% after 2000 cycles	This work
SnS_2	1081 mAh g^{-1} at 0.2 A g^{-1}	86.0% after 30 cycles	[34]
$SnSe_2$ QDs/rGO	778.5 mAh g^{-1} at 50 mA g^{-1}	92.2% after 3000 cycles	[38]
SnS_2/NRGO	588 mAh g^{-1} at 0.2 A g^{-1}	95.6% after 200 cycles	[42]
SnS/NRGO	434 mAh g^{-1} at 0.2 A g^{-1}	52.8% after 200 cycles	[42]
SnS_2@GF	948.4 mAh g^{-1} at 0.1 A g^{-1}	86.3% after 500 cycles	[43]
CPN@SnS_2	1353 mAh g^{-1} at 60 mA g^{-1}	49.2% after 100 cycles	[44]
MoS_2@SnO_2–SnS/C	1006 mAh g^{-1} at 0.2 A g^{-1}	63.2% after 500 cycles	[45]
SnS/MoS_2–C	1002 mAh g^{-1} at 0.2 A g^{-1}	~100% after 700 cycles	[46]
$SnSe_{0.5}S_{0.5}$/C	989 mAh g^{-1} at 0.1 A g^{-1}	63.2% after 500 cycles	[47]
SnSe NPs	920 mAh g^{-1} at 0.2 A g^{-1}	86.8% after 100 cycles	[48]
$SnS_{0.9}Se_{0.1}$@CNFs	924 mAh g^{-1} at 0.2 A g^{-1}	75% after 100 cycles	[49]

SnSSe electrode. Fig. 4d reveals the CV curves of SnSSe/rGO electrode at different scan rates. Four peak groups *a-d* are labeled to verify the lithiation-type of SnSSe/rGO electrode. The equation of $\log(i) = m^*\log(v) + \log(n)$, in which i represents the peak current, v represents the scan rate, and m and n represent the adjustable values, can be used to determine the Li^+-diffusion lithiation type instead of pseudocapacitive behavior if the value of m approaches 0.5 instead of 1.0. Fig. 4e displays the linear-fitting curves of log(v) and log(i), and the simulated m values of peak groups *a-d* are separately 0.70, 0.58, 0.60, and 0.72 (Table S2, Supporting Information). Therefore, the Li^+-diffusion mechanism dominates the electrochemical behavior [53]. The schematic of facile Li^+ diffusion in the SnSSe/rGO electrode is illustrated in Fig. 4f. The contoured rGO nanolayer conforms to the SnSSe nanosheets with an ordered layered orientation, which allows facile Li^+ diffusion channels compared to that of the disordered configuration of SnSSe

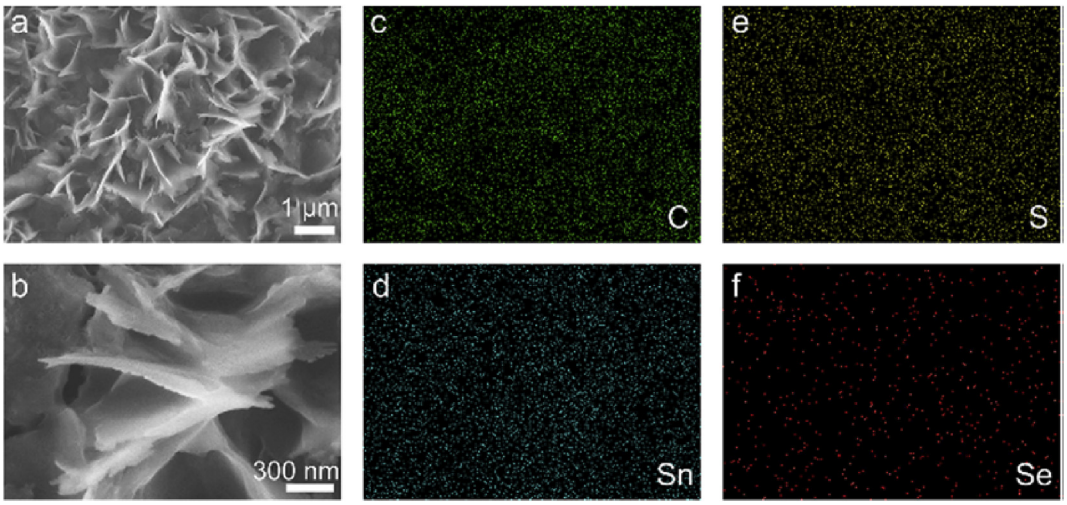

Fig. 5. Characterizations of the morphology and surface elements of the long-life cycled SnSSe/rGO electrode. SEM (a) and HRSEM (b) images of the SnSSe/rGO electrode after the long-life cycling process tested at 1 A g^{-1}. (c–f) EDX elemental mapping images of the SnSSe/rGO electrode after the long-life cycling process tested at 1 A g^{-1}.

nanosheets. Therefore, the oriented growth of layered facets in the SnSSe nanosheets with an extensive exposure of Li^+-diffusion channels, together with the effective accommodation to volume expansion–contraction and the excellent electronic conductivity provided by the rGO matrix, ensure the long-term cycling stability and high capacity delivery.

The morphology of long-life cycled SnSSe/rGO electrode was characterized by SEM. As shown in Fig. 5a, open lamellas appear on the electrode surface and their interconnections form the vertical flower-like morphology. The fine morphology of open lamellas are revealed in Fig. 5b. The average thickness of open lamellas is less than 100 nm and their surfaces extend smoothly along with the direction of Li^+ diffusion. This special open structure can provide more active sites and buffer the volume change of SnSSe nanosheets during the discharge/charge processes. The EDX technology confirms the elemental distributions (the corresponding SEM image is exhibited in Fig. S13, Supporting Information). As shown in Fig. 5c–f, the EDX elemental mapping images demonstrate that the C, Sn, S, and Se elements all reveal uniform distributions. Therefore, the open lamellas are still integrated with the rGO matrix and tin chalcogenides.

4. Conclusions

In summary, layered SnSSe nanosheets are synthesized by using a simple solid-state reaction and then a wet ball-milling method. They feature the oriented growth of (001) facet that breaks the shackle of strong competition from the (101) and (011) facets in the tin-based LMCs, thus allowing facile Li^+-diffusion channels. A further construction with rGO conductive matrix enables the flexible freestanding SnSSe/rGO electrodes with an order-stacked framework, which is assembled with the tiled SnSSe nanosheets and the planar extended rGO nanolayers. A superior specific capacity delivery of 2049 mAh g^{-1} is realized at 0.1 A g^{-1} for the active mass of SnSSe, and an excellent capacity retention of 82% is also delivered at 1 A g^{-1} even after 2000 cycles. An open structure with vertical lamellas is characterized on the surface of long-life cycled electrode. Tailoring desirable crystal facets to build better electrode materials for LIBs and other battery systems can be envisioned in view of its high feasibility.

Acknowledgements

This work was supported by the Strategic Priority Research Program of the Chinese Academy of Sciences (XDA21010214), the National Key Research and Development Program of China (2016YFB0700604), the National Natural Science Foundation of China of China (21622407, 21875266, 21673008) and the Shenzhen Science and Technology Research Grant (JCYJ20170412150450297).

Appendix A. Supplementary data

Supplementary data to this article can be found online at https://doi.org/10.1016/j.electacta.2019.06.041.

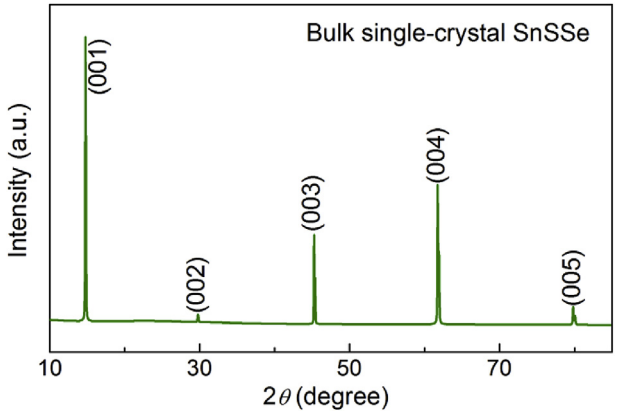

Fig. S1. XRD pattern of the single-crystal SnSSe. Only the layered-structure-related (00*l*) peaks are demonstrated.

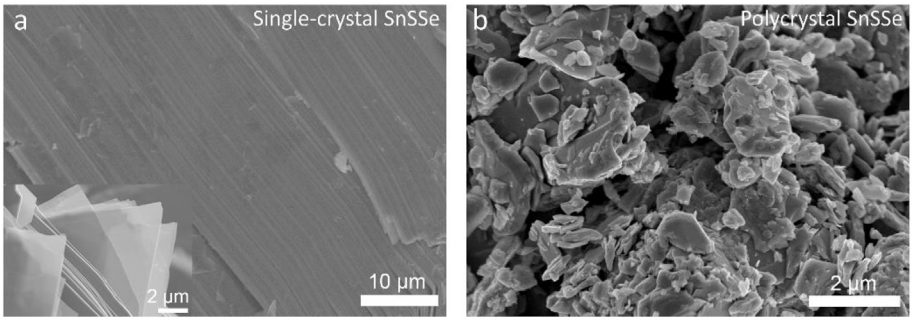

Fig. S2. SEM images of the single-crystal SnSSe (a) and polycrystal SnSSe (b). The inset in panel (a) shows the front SEM image of single-crystal SnSSe. Typical layered configuration is revealed in the single-crystal SnSSe.

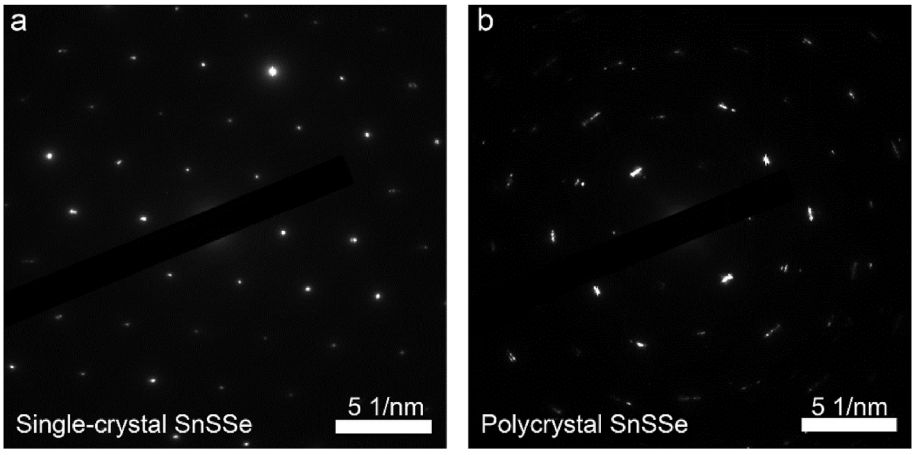

Fig. S3. SAED patterns of the single-crystal SnSSe (a) and polycrystal SnSSe (b).

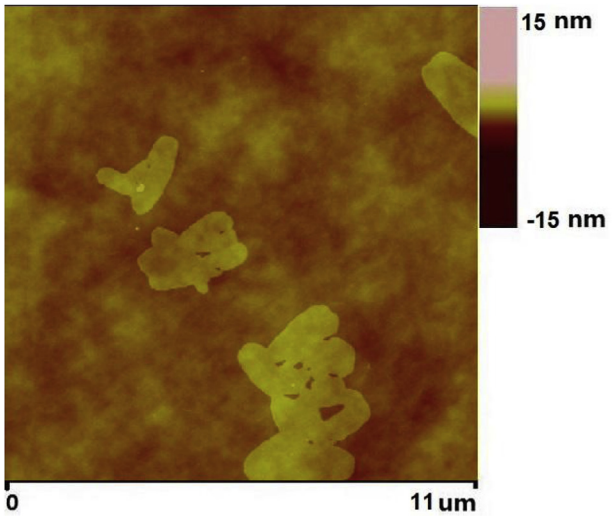

Fig. S4. AFM topography image of the SnSSe nanosheets. The thickness of SnSSe nanosheets is below 2 nm.

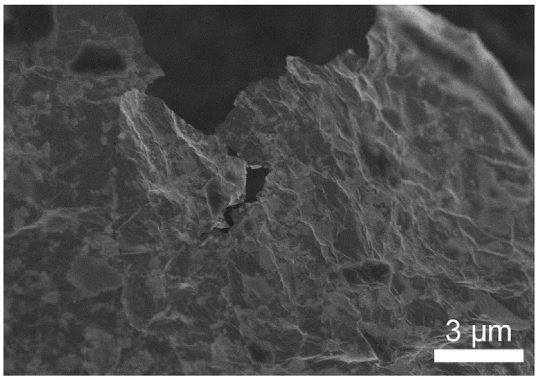

Fig. S5. Front SEM image of the SnSSe/rGO. The SnSSe nanosheets show a tiled way on the surface of rGO.

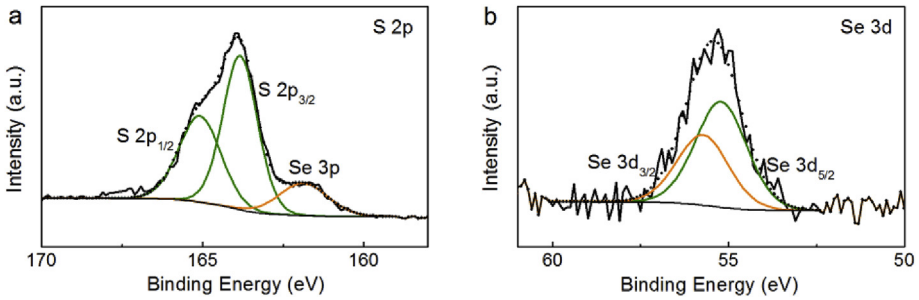

Fig. S6. S 2p region (a) and Se 3d region (b) in the XPS spectrum of SnSSe/rGO.

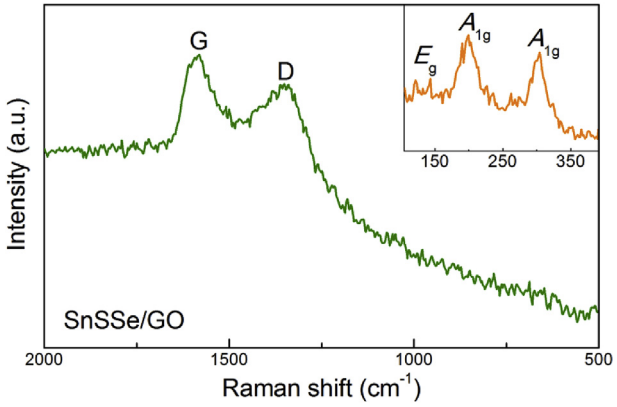

Fig. S7. Raman pattern of the SnSSe/GO before the reduction process. The intensity ratio of D (1350 cm^{-1}) and G (1586 cm^{-1}) peaks (I_D/I_G) in the SnSSe/GO is fitted to be 0.90. The inset shows the characteristic Raman peaks of SnSSe.

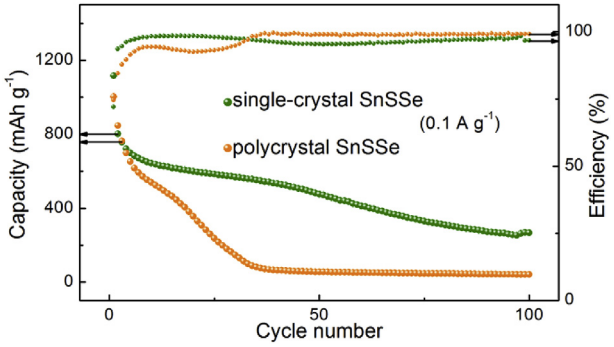

Fig. S8. Cycling performance of the single-crystal SnSSe and polycrystal SnSSe electrodes tested at 0.1 A g^{-1}.

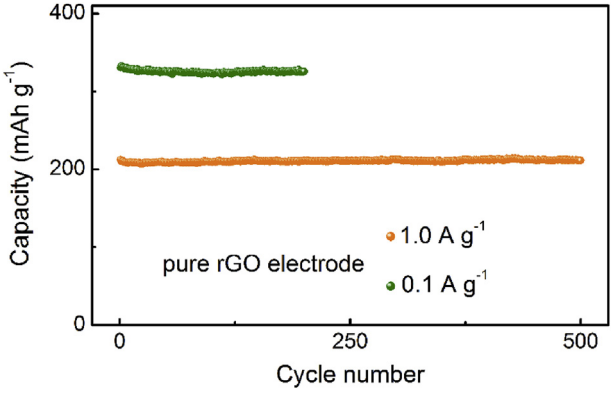

Fig. S9. Cycling performance of the rGO electrodes tested at 0.1 and 1.0 A g^{-1}. Stable capacity deliveries are demonstrated at both the 0.1 and 1.0 A g^{-1} with the average values of 326 and 211 mAh g^{-1}, respectively.

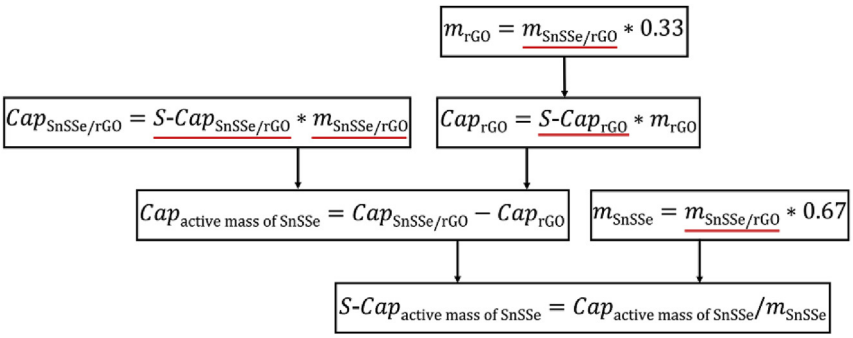

Fig. S10. Specific formulas of calculating the specific capacity (mAh g^{-1}) of active mass of SnSSe. *m*, *Cap*, and *S-Cap* represent the mass (g), capacity (mAh), and specific capacity (mAh g^{-1}), respectively, and the red underlines represent the known quantities. The values of $S\text{-}Cap_{rGO}$ adopt 326 and 211 mAh g^{-1} at 0.1 and 1.0 A g^{-1}, respectively.

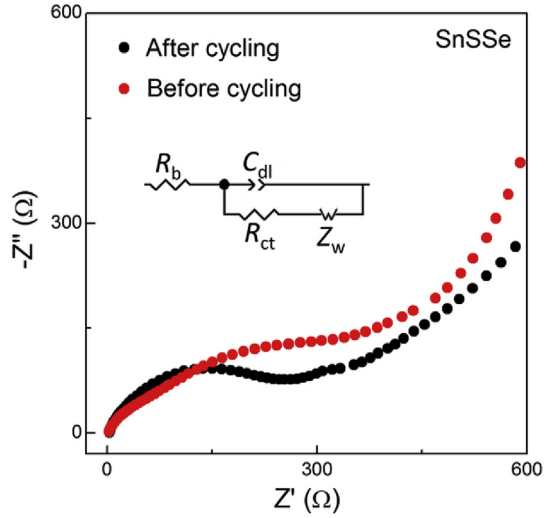

Fig. S11. EIS patterns of the SnSSe electrode before and after cycling. The inset is the corresponding equivalent circuit.

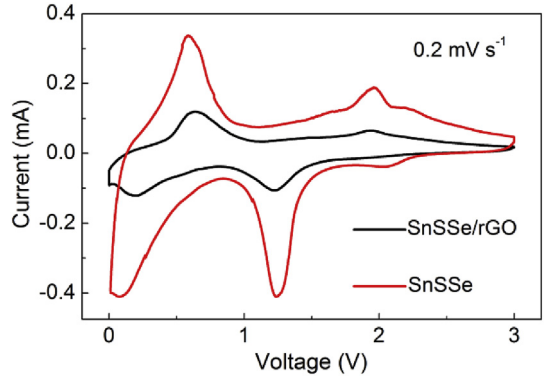

Fig. S12. CV curves of the SnSSe and SnSSe/rGO electrodes performed at 0.2 mV s^{-1}.

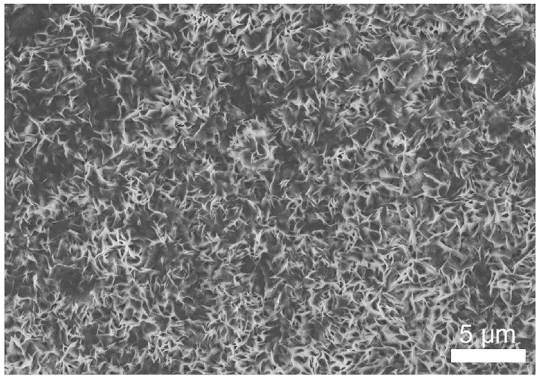

Fig. S13. SEM image of the long-life cycled SnSSe/rGO electrode collected for the EDX test.

Table S1
Comparison of the fitted R_{ct} values of SnSSe/rGO and SnSSe electrodes before and after cycling.

Electrode	SnSSe/rGO (before cycling)	SnSSe/rGO (after cycling)	SnSSe (before cycling)	SnSSe (after cycling)
R_{ct} value (Ω)	69	46	618	311

Table S2
Specific values of *m* and *n* for peak groups *a*-*d*.

Peak group	*a*	*b*	*c*	*d*
m	0.70	0.58	0.60	0.72
n	−0.51	−0.47	−0.55	−0.70

The power-law relationship can be described as $i = n^* v^m$, in which *i* is the current, *v* is the scan rate, and *m* and *n* are two adjustable parameters. The above formula can be deformed into $\log(i) = m^*\log(v) + \log(n)$ to obtain the values of *m* and *n*, through collecting the peak currents and scan rates of peak groups *a*-*d*.

References

[1] A. Gurung, K. Chen, R. Khan, S.S. Abdulkarim, G. Varnekar, R. Pathak, R. Naderi, Q. Qiao, Highly efficient perovskite solar cell photocharging of lithium ion battery using DC–DC booster, Adv. Energy Mater. 7 (2017) 1602105.

[2] S.J.P. Varapragasam, C. Balasanthiran, A. Gurung, Q. Qiao, R.M. Rioux, J.D. Hoefelmeyer, Kirkendall growth of hollow Mn_3O_4 nanoparticles upon galvanic reaction of MnO with Cu^{2+} and evaluation as anode for lithium-ion batteries, J. Phys. Chem. C 121 (2017) 11089–11099.

[3] M. McGraw, P. Kolla, B. Yao, R. Cook, Q. Quiao, J. Wu, A. Smirnova, One-step solid-state in-situ thermal polymerization of silicon-PEDOT nanocomposites for the application in lithium-ion battery anodes, Polymer 99 (2016) 488–495.

[4] Z. Zhou, H. Zhang, Y. Zhou, H. Qiao, A. Gurung, R. Naderi, H. Elbohy, A.L. Smirnova, H. Lu, S. Chen, Q. Qiao, Binder free hierarchical mesoporous carbon foam for high performance lithium ion battery, Sci. Rep. 7 (2017) 1440.

[5] R. Naderi, A. Gurung, Z. Zhou, G. Varnekar, K. Chen, J. Zai, X. Qian, Q. Qiao, Activation of passive nanofillers in composite polymer electrolyte for higher performance lithium-ion batteries, Adv. Sustain. Syst. 1 (2017) 1700043.

[6] M. Gao, Y. Xu, J. Jiang, S. Yu, Nanostructured metal chalcogenides: synthesis, modification, and applications in energy conversion and storage devices, Chem. Soc. Rev. 42 (2013) 2986–3017.

[7] N. Nitta, F. Wu, J.T. Lee, G. Yushin, Li-ion battery materials: present and future, Mater. Today 18 (2015) 252–264.

[8] X. Wang, Z. Yang, C. Wang, L. Ma, C. Zhao, J. Chen, X. Zhang, M. Xue, Auto-generated iron chalcogenide microcapsules ensure high-rate and high-capacity sodium-ion storage, Nanoscale 10 (2018) 800–806.

[9] H. Hwang, H. Kim, J. Cho, MoS_2 nanoplates consisting of disordered graphene-like layers for high rate lithium battery anode materials, Nano Lett. 11 (2011) 4826–4830.

[10] R. Bhandavat, L. David, G. Singh, Synthesis of surface-functionalized WS_2 nanosheets and performance as Li-ion battery anodes, J. Phys. Chem. Lett. 3 (2012) 1523–1530.

[11] J.W. Seo, J.T. Jang, S.W. Park, C. Kim, B. Park, J. Cheon, Two-dimensional SnS_2 nanoplates with extraordinary high discharge capacity for lithium ion batteries, Adv. Mater. 20 (2008), 4269–42.

[12] A. Gurung, R. Naderi, B. Vaagensmith, G. Varnekar, Z. Zhou, H. Elbohy, Q. Qiao, Tin selenide–multi-walled carbon nanotubes hybrid anodes for high performance lithium-ion batteries, Electrochim. Acta 211 (2016) 720–725.

[13] F. Xiong, H. Wang, X. Liu, J. Sun, M. Brongersma, E. Pop, Y. Cui, Li intercalation in MoS_2: in situ observation of its dynamics and tuning optical and electrical properties, Nano Lett. 15 (2015) 6777–6784.

[14] X. Wang, Z. Yang, C. Wang, D. Chen, R. Li, X. Zhang, J. Chen, M. Xue, Buffer layer enhanced stability of sodium-ion storage, J. Power Sources 369 (2017) 138–145.

[15] D. Chen, X. Wang, J. Chen, Z. Ren, M. Xue, G. Chen, Rewriting the superconductivity in iron-based superconductors by lithium-ion insertion and extraction, Adv. Mater. 27 (2015) 4224–4228.

[16] X. Wang, K. Du, C. Wang, L. Ma, B. Zhao, J. Yang, M. Li, X.X. Zhang, M. Xue, J. Chen, Unique reversible conversion-type mechanism enhanced cathode performance in amorphous molybdenum polysulfide, ACS Appl. Mater. Interfaces 9 (2017) 38606–38611.

[17] Y. Liu, X. Wang, X. Song, Y. Dong, L. Yang, L. Wang, D. Jia, Z. Zhao, J. Qiu, Interlayer expanded MoS_2 enabled by edge effect of graphene nanoribbons for high performance lithium and sodium ion batteries, Carbon 109 (2016) 461–471.

[18] X. Wang, Z. Zhang, Y. Chen, Y. Qu, Y. Lai, J. Li, Morphology-controlled synthesis of MoS_2 nanostructures with different lithium storage properties, J. Alloy. Comp. 600 (2014) 84–90.

[19] Z. Deng, H. Jiang, Y. Hu, Y. Liu, L. Zhang, H. Liu, C. Li, 3D ordered macroporous MoS_2@C nanostructure for flexible Li-ion batteries, Adv. Mater. 29 (2017) 1603020.

[20] Z. Liu, H. Deng, P.P. Mukherjee, Evaluating pristine and modified SnS_2 as a lithium-ion battery anode: a first-principles study, ACS Appl. Mater. Interfaces 7 (2015) 4000–4009.

[21] M. Wu, J. Zhan, K. Wu, Z. Li, L. Wang, B. Geng, L. Wang, D. Pan, Metallic 1T MoS_2 nanosheet arrays vertically grown on activated carbon fiber cloth for enhanced Li-ion storage performance, J. Mater. Chem. 5 (2017) 14061–14069.

[22] J. Shao, Q. Qu, Z. Wan, T. Gao, Z. Zuo, H. Zheng, From dispersed microspheres to interconnected nanospheres: carbon-sandwiched monolayered MoS_2 as high-performance anode of Li-ion batteries, ACS Appl. Mater. Interfaces 7 (2015) 22927–22934.

[23] S. Zhang, B.V.R. Chowdari, Z. Wen, J. Jin, J. Yang, Constructing highly oriented configuration by few-layer MoS_2: toward high-performance lithium-ion batteries and hydrogen evolution reactions, ACS Nano 9 (2015) 12464–12472.

[24] F. Sun, Y. Wei, J. Chen, D. Long, L. Ling, Y. Li, J. Shi, Melamine-assisted one-pot synthesis of hierarchical nitrogen-doped carbon@MoS2 nanowalled core–shell microspheres and their enhanced Li-storage performances, Nanoscale 7 (2015) 13043–13050.

[25] K. Chang, W. Chen, L. Ma, H. Li, F. Huang, Z. Xu, Q. Zhang, J. Lee, Graphene-like MoS_2/amorphous carbon composites with high capacity and excellent stability as anode materials for lithium ion batteries, J. Mater. Chem. 21 (2011) 6251–6257.

[26] Y. Xue, Q. Zhang, W. Wang, H. Cao, Q. Yang, L. Fu, Opening two-dimensional materials for energy conversion and storage: a concept, Adv. Energy Mater. 7 (2017) 1602684.

[27] H. Jiang, D. Ren, H. Wang, Y. Hu, S. Guo, H. Yuan, P. Hu, L. Zhang, C. Li, 2D monolayer MoS2–carbon interoverlapped superstructure: engineering ideal atomic interface for lithium ion storage, Adv. Mater. 27 (2015) 3687–3695.

[28] K. Zhou, Y. Li, Catalysis based on nanocrystals with well-defined facets, Angew. Chem. Int. Ed. 51 (2012) 602–613.

[29] S. Liu, J. Yu, M. Jaroniec, Tunable photocatalytic selectivity of hollow TiO_2 microspheres composed of anatase polyhedra with exposed {001} facets, J. Am. Chem. Soc. 132 (2010) 11914–11916.

[30] X. Han, M. Jin, S. Xie, Q. Kuang, Z. Jiang, Y. Jiang, Z. Xie, L. Zheng, Synthesis of tin dioxide octahedral nanoparticles with exposed high-energy {221} facets and enhanced gas-sensing properties, Angew. Chem. 121 (2009) 9344–9347.

[31] M. Xue, Y. Wang, X. Wang, X. Huang, J. Ji, Single-crystal-conjugated polymers with extremely high electron sensitivity through template-assisted in situ polymerization, Adv. Mater. 27 (2015) 5923–5929.

[32] S. Liu, X. Lu, J. Xie, G. Cao, T. Zhu, X. Zhao, Preferential *c*-Axis orientation of ultrathin SnS_2 nanoplates on graphene as high-performance anode for Li-ion batteries, ACS Appl. Mater. Interfaces 5 (2013) 1588–1595.

[33] F. Zhang, C. Xia, J. Zhu, B. Ahmed, H. Liang, D.B. Velusamy, U. Schwingenschlögl, H.N. Alshareef, $SnSe_2$ 2D anodes for advanced sodium ion batteries, Adv. Energy Mater. 6 (2016) 1601188.

[34] Y. Du, Z. Yin, X. Rui, Z. Zeng, X. Wu, J. Liu, Y. Zhu, J. Zhu, X. Huang, Q. Yan, H. Zhang, A facile, relative green, and inexpensive synthetic approach toward large-scale production of SnS_2 nanoplates for high-performance lithium-ion batteries, Nanoscale 5 (2013) 1456–1459.

[35] X. Zang, X. Wang, Z. Yang, X. Wang, R. Li, J. Chen, J. Ji, M. Xue, Unprecedented sensitivity towards pressure enabled by graphene foam, Nanoscale 9 (2017) 19346–19352.

[36] X. Wang, D. Chen, Z. Yang, X. Zhang, C. Wang, J. Chen, X. Zhang, M. Xue, Novel metal chalcogenide SnSSe as a high-capacity anode for sodium-ion batteries, Adv. Mater. 28 (2016) 8645–8650.

[37] Z. Yang, H. Liang, X. Wang, X. Ma, T. Zhang, Y. Yang, L. Xie, D. Chen, Y. Long, J. Chen, Y. Chang, C. Yan, X. Zhang, X. Zhang, B. Ge, Z. Ren, M. Xue, G. Chen, Atom-thin $SnS_{2-x}Se_x$ with adjustable compositions by direct liquid exfoliation from single crystals, ACS Nano 10 (2016) 755–762.

[38] Z. Huang, B. Liu, D. Kong, Y. Wang, H. Yang, $SnSe_2$ Quantum Dot/rGO composite as high performing lithium anode, Energy Storage Mater. 10 (2018) 92–101.

[39] B. Wang, Z. Wen, J. Jin, X. Hong, S. Zhang, K. Rui, A novel strategy to prepare Ge@C/rGO hybrids as high-rate anode materials for lithium ion batteries, J. Power Sources 342 (2017) 521–528.

[40] A.K. Garg, Concentration dependent vibrational mode behaviour in the mixed crystal system SnS_xSe_{2-x}, J. Mol. Struct. 247 (1991) 47–60.

[41] M.K. Jana, H.B. Rajendra, A.J. Bhattacharyya, K. Biswas, Green ionothermal synthesis of hierarchical nanostructures of SnS_2 and their Li-ion storage properties, CrystEngComm 16 (2014) 3994–4000.

[42] D.H. Youn, S.K. Stauffer, P. Xiao, H. Park, Y. Nam, A. Dolocan, G. Henkelman, A. Heller, C.B. Mullins, Simple synthesis of nanocrystalline tin sulfide/N-doped reduced graphene oxide composites as lithium ion battery anodes, ACS Nano 10 (2016) 10778–10788.

[43] Y. Ren, W. Lv, F. Wen, J. Xiang, Z. Liu, Microwave synthesis of SnS_2 nanoflakes anchored graphene foam for flexible lithium-ion battery anodes with long cycling life, Mater. Lett. 174 (2016) 24–27.

[44] X. Chen, Y. Huang, K. Zhang, X. Feng, M. Wang, Synthesis and high-

performance of carbonaceous polypyrrole nanotubes coated with SnS_2 nanosheets anode materials for lithium ion batteries, Chem. Eng. J. 330 (2017) 470–479.
[45] Q. Pan, F. Zheng, X. Ou, C. Yang, X. Xiong, M. Liu, MoS_2 encapsulated SnO_2-SnS/C nanosheets as a high performance anode material for lithium ion batteries, Chem. Eng. J. 316 (2017) 393–400.
[46] Q. Pan, F. Zheng, Y. Wu, X. Ou, C. Yang, X. Xiong, M. Liu, MoS_2-covered SnS nanosheets as anode material for lithium-ion batteries with high capacity and long cycle life, J. Mater. Chem. 6 (2018) 592–598.
[47] Q. Tang, Y. Cui, J. Wu, D. Qu, A.P. Baker, Y. Ma, X. Song, Y. Liu, Ternary tin selenium sulfide ($SnSe_{0.5}S_{0.5}$) nano alloy as the high-performance anode for lithium-ion and sodium-ion batteries, Nano Energy 41 (2017) 377–386.
[48] W. Wang, P. Li, H. Zheng, Q. Liu, F. Lv, J. Wu, H. Wang, S. Guo, Ultrathin layered SnSe nanoplates for low voltage, high-rate, and long-life alkali–ion batteries, Small 13 (2017) 1702228.
[49] L. Lu, L. Zhang, H. Zeng, B. Xu, L. Wang, Y. Li, Enhanced cycling performance of Se-doped SnS carbon nanofibers as negative electrode for lithium-ion batteries, J. Alloy. Comp. 695 (2017) 1294–1300.
[50] R. Pathak, A. Gurung, H. Elbohy, K. Chen, K.M. Reza, B. Bahrami, S. Mabrouk, R. Ghimire, M. Hummel, Z. Gu, X. Wang, Y. Wu, Y. Zhou, Q. Qiao, Self-recovery in Li-metal hybrid lithium-ion batteries via WO_3 reduction, Nanoscale 10 (2018) 15956–15966.
[51] K. Chen, R. Pathak, A. Gurung, E.A. Adhamash, B. Bahrami, Q. He, H. Qiao, A.L. Smirnova, J.J. Wu, Q. Qiao, Y. Zhou, Flower-shaped lithium nitride as a protective layer via facile plasma activation for stable lithium metal anodes, Energy Storage Mater. 18 (2019), 389–6.
[52] X. Jiang, X. Yang, Y. Zhu, J. Shen, K. Fan, C. Li, In situ assembly of graphene sheets-supported SnS_2 nanoplates into 3D macroporous aerogels for high-performance lithium ion batteries, J. Power Sources 237 (2013) 178–186.
[53] C. Liu, X. Wang, W. Deng, C. Li, J. Chen, M. Xue, R. Li, F. Pan, Engineering fast ion conduction and selective cation channels for a high-rate and high-voltage hybrid aqueous battery, Angew. Chem. Int. Ed. 57 (2018) 7046–7050.